FERROELECTRICS

Emergent helical texture of electric dipoles

Dmitry D. Khalyavin[1]*, Roger D. Johnson[2,3], Fabio Orlandi[1], Paolo G. Radaelli[3], Pascal Manuel[1], Alexei A. Belik[4]

Long-range ordering of magnetic dipoles in bulk materials gives rise to a broad range of magnetic structures, from simple collinear ferromagnets and antiferromagnets, to complex magnetic helicoidal textures stabilized by competing exchange interactions. In contrast, dipolar order in dielectric crystals is typically limited to parallel (ferroelectric) and antiparallel (antiferroelectric) collinear alignments of electric dipoles. Here, we report an observation of incommensurate helical ordering of electric dipoles by light hole doping of the quadruple perovskite $BiMn_7O_{12}$. In analogy with magnetism, the electric dipole helicoidal texture is stabilized by competing instabilities. Specifically, orbital ordering and lone electron pair stereochemical activity compete, giving rise to phase transitions from a nonchiral cubic structure to an incommensurate electric dipole and orbital helix via an intermediate density wave.

The long-range ordering of magnetic and/or electric dipoles is a canonical cause of phase transitions in crystalline materials and is associated with a variety of functional properties. Despite the fundamentally different nature of the interactions between magnetic and electric dipoles, there are many similarities between the two types of phase transition, as first mentioned by Valasek (*1*) in 1922. In particular, many materials display parallel dipole alignments (as in ferromagnets and ferroelectrics) or antiparallel dipole alignments (as in antiferromagnets and antiferroelectrics). First predicted theoretically by Néel in 1948 (*2*), antiferromagnetic spin ordering was experimentally confirmed in MnO one year later using the newly established neutron diffraction technique (*3*), a discovery that led to rapid experimental and theoretical developments (*4*). Antiferroelectricity was first proposed in $PbZrO_3$ by Sawaguchi, Maniwa, and Hoshino in 1951 (*5*) on the basis of the antiparallel displacements of Pb established by x-ray diffraction. Although by far the most common, collinear ferro-dipolar and antiferro-dipolar orderings (as well as their simple combinations such as ferri-structures and canted structures) are not the only possibilities. In the late 1950s and early 1960s, Koehler *et al.* (*6*, *7*) and Yoshimori (*8*) discovered the first examples of noncollinear helical magnetic ordering in Ho and other rare earth metals, as well as in rutile MnO_2.

Nowadays, many exotic orderings of magnetic dipoles are known, where spins gradually rotate creating complex patterns whose period is often incommensurate with the crystal structure. Such spin textures, characterized by additional macroscopic quantities such as chirality and polarity, play a central role in the physics of multiferroic materials, frustrated magnetism, skyrmions, and magnetic domain walls. By analogy, one could expect that helical ordering should also occur in materials containing electric dipoles. However, such electric dipole textures have been challenging to observe experimentally in a bulk material. Here, we report an example of incommensurate helical ordering of electric dipoles in the lightly doped quadruple perovskite $BiCu_xMn_{7-x}O_{12}$. In addition to completing the analogy between ordering of magnetic and electric dipoles, our discovery demonstrates that many principles of noncollinear magnetism can be adopted to understand the properties of dielectric materials.

The parent compound $BiMn_7O_{12}$ is a so-called quadruple perovskite with Mn^{3+} on both A and B perovskite sites, $[BiMn^{3+}{}_3]_A[Mn^{3+}{}_4]_BO_{12}$. It combines two well-known electronic instabilities, leading to a complex structural behavior (*9*): the stereochemical activity of Bi^{3+} caused by the $6s^2$ lone-pair electrons, and the Jahn-Teller (JT) instability caused by the degenerate e_g electronic states of octahedrally coordinated Mn^{3+}. The former promotes off-centric cation displacements and the formation of local electric dipoles (*10*) and is thus responsible for the ferroelectric properties of many Bi-containing perovskite oxides (*11*–*13*). The latter often results in a structural phase transition characterized by a coherent, spontaneous distortion of polyhedra coordinating Mn^{3+}, for instance, as in the case of $LaMnO_3$ (*14*). At high temperatures, $BiMn_7O_{12}$ adopts a cubic nonferroelectric structure with space group (SG) *Im-3*, whereas upon cooling it undergoes three distinct structural transitions at temperatures T_{JT} ~ 608 K, T_C ~ 460 K, and T_S ~ 290 K. The highest-temperature transition at T_{JT} (to SG *I*2/*m*) is driven by cooperative JT distortions, leading to a B-site orbital pattern identical to the prototype manganite $LaMnO_3$ (*14*). At the Curie temperature T_C, $BiMn_7O_{12}$ becomes ferroelectric owing to ferro-dipolar ordering of the Bi lone pairs, whereas the crystallographic transition at T_S is between the higher-temperature (SG *Im*) and ground-state (SG *P*1) ferroelectric phases. This transition can be interpreted as an electric dipole reorientation at which the electric polarization (initially confined within the *ac* plane) rotates to a general direction (*15*). Throughout both ferroelectric phases, the $LaMnO_3$-type orbital order remains largely unchanged.

As is the case for other manganites (*16*, *17*), a small amount of hole doping achieved, for example, by the replacement of A-site Mn^{3+} with Cu^{2+}, is expected to tune both instabilities because it affects both the JT ordering [doped holes are localized on B sites (*18*, *19*) such that Mn^{3+} tends toward non-JT-active Mn^{4+}] and the immediate coordination of Bi^{3+}. Similar to the undoped compound, $BiCu_{0.1}Mn_{6.9}O_{12}$ is cubic at high temperatures [structural parameters for this phase as well as for the phases discussed below are summarized in tables S1 to S5 and figs. S1 to S8 (*20*)] and undergoes a JT-order phase transition to the nonpolar monoclinic structure with SG *I*2/*m* at a slightly lower T_{JT} of ~560 K (Fig. 1A and fig. S3) accompanied by the same $LaMnO_3$-type orbital order.

The nature of the two lower-temperature phase transitions in $BiCu_{0.1}Mn_{6.9}O_{12}$ is notably different than in $BiMn_7O_{12}$ (Fig. 1A and figs. S4 to S6). The Curie and structural transitions are replaced by transitions to two incommensurately modulated phases at T_{I1} ~ 435 K and T_{I2} ~ 390 K, both of which are described below. The transitions are strongly first-order and are associated with large thermal hysteresis (fig. S9). In both modulated phases, the incommensurate satellite reflections observed in the diffraction patterns (Fig. 1B and figs. S4 and S5) are very strong. These sudden structural changes at such low doping strongly suggest that the modulation can be associated with reconstruction of the primary electronic instabilities, namely, ferroelectric dipole ordering and/or orbital polarization.

Crystallographic analysis performed at T = 427 K (below T_{I1}) revealed that the structure is metrically triclinic with the incommensurate modulation vector $\boldsymbol{k}_{HT}$ = (−0.0037(8), 0.026(1), 0.1233(8))—approximately parallel to the body diagonal of the pseudocubic cell. Structural refinements performed in the *R*-1($\alpha\beta\gamma$)0 superspace group (SSG) established that the Bi cations predominantly shift along the *a* axis (former cubic [0-11]$_C$ direction) (Fig. 2A) and adopt the largest modulation amplitude of all atomic species. The large displacements of Bi confirm that the modulation is related to the ordering of lone electron pairs, which in the parent material, $BiMn_7O_{12}$, induces ferroelectricity by adopting parallel ordering. In contrast, in the triclinic

[1]ISIS Facility, Rutherford Appleton Laboratory, Harwell Campus, Didcot OX11 0QX, UK. [2]Department of Physics and Astronomy, University College London, London WC1E 6BT, UK. [3]Department of Physics, University of Oxford, Oxford OX1 3PU, UK. [4]International Center for Materials Nanoarchitectonics (WPI-MANA), National Institute for Materials Science (NIMS), Namiki 1-1, Tsukuba, Ibaraki 305-0044, Japan.
*Corresponding author. Email: dmitry.khalyavin@stfc.ac.uk

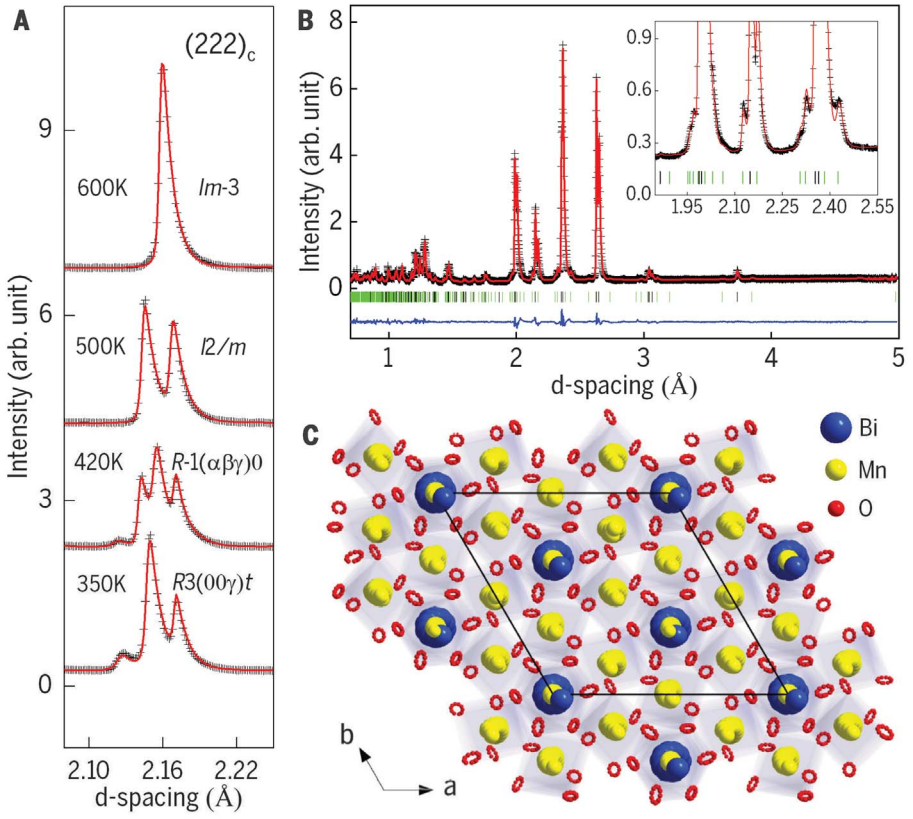

Fig. 1. Crystal structure refinement. (**A**) Thermal evolution of $(222)_c$ fundamental reflection measured by neutron diffraction in the different phases of $BiCu_{0.1}Mn_{6.9}O_{12}$. arb. unit, arbitrary unit. (**B**) Rietveld refinement of the neutron diffraction data collected at room temperature in the modulated helical phase. Cross symbols and solid red line represent experimental and calculated intensities, respectively, and the blue line below is the difference between them. The black tick marks indicate positions of the fundamental peaks, and the green tick marks indicate positions of the satellites. The corresponding structural parameters are listed in table S4. The inset shows a region where the strongest satellite reflections are observed in the modulated helical phase. (**C**) View along the *c* axis of the crystal structure of $BiCu_{0.1}Mn_{6.9}O_{12}$ in the modulated helical phase, demonstrating chiral atomic displacements. For simplicity, all sites occupied by transition metals are labeled as Mn and colored yellow. In the studied material, ~3% of the A-site Mn is substituted with Cu.

phase of $BiCu_{0.1}Mn_{6.9}O_{12}$, the Bi displacements are aligned on a fixed axis, but their amplitude is modulated giving zero net ferroelectric polarization. This electric dipole ordering strongly resembles the incommensurate structure of magnetic moments in a spin density wave (SDW), which is a feature of many magnetic systems with frustrated exchange interactions. Our triclinic dipole density wave (DDW) structure is stable only in a narrow temperature range below the phase transition—another point of similarity with SDWs in insulators, where this type of magnetic ordering is almost always entropically stabilized.

The low-temperature phase of $BiCu_{0.1}Mn_{6.9}O_{12}$, below T_{12} ~ 390 K and down to the ground state, is metrically trigonal and heavily modulated along the *c* axis; $\boldsymbol{k}_{LT} = (0,0,\gamma)$ with $\gamma = 0.1046(5)$ at $T = 380$ K. This modulation vector is on the Λ line of symmetry and is oriented exactly along the body diagonal of the pseudocubic cell [$\boldsymbol{k}_{LT} = (2/3\gamma,2/3\gamma,2/3\gamma)$ in the *Im*-3 setting]. A systematic test of all isotropy subgroups of *Im*-3 associated with this type of modulation (*21*–*23*) revealed that only the noncentrosymmetric SSG $R3(00\gamma)t$ can provide an excellent refinement quality for both neutron (Fig. 1B) and x-ray (fig. S5) diffraction patterns. The obtained crystal structure comprises a distinct pattern of modulated distortions (Fig. 1C). The largest refined atomic displacements are, once again, associated with Bi and lie in the *ab* plane of the trigonal cell, and all have the same amplitude of 0.41(1) Å at $T = 300$ K. This value is extremely large: It exceeds the ferroelectric displacements of the cations in the undoped $BiMn_7O_{12}$ (~0.37 Å) (*9*, *24*) and $BiFeO_3$ (~0.40 Å) (*25*).

In the lower-temperature phase of $BiCu_{0.1}Mn_{6.9}O_{12}$ ($T < 390$ K), the displacement vectors rotate perpendicular to the modulation wave vector propagating along the *c* axis (Figs. 1C and 2, B and C) and are therefore the structural analog of a magnetic incommensurate proper helix. Thus, in this phase, the lone electron pairs of Bi^{3+} cations are ordered into a helical structure, making $BiCu_{0.1}Mn_{6.9}O_{12}$ a textbook example of a helical texture of electric dipoles. In general, the order parameter of a structural or magnetic helical phase can be defined as a mixed product $\sigma_s = \boldsymbol{k}_{LT}\cdot[\boldsymbol{r}_i \times \boldsymbol{r}_j]$ or $\sigma_m = \boldsymbol{k}_m\cdot[\boldsymbol{S}_i \times \boldsymbol{S}_j]$, where $\boldsymbol{r}_i$ and $\boldsymbol{r}_j$ ($\boldsymbol{S}_i$ and $\boldsymbol{S}_j$) are atomic displacements (spins) in adjacent unit cells along the propagation vector $\boldsymbol{k}_{LT}$ ($\boldsymbol{k}_m$) (Fig. 2, B and C). In both cases, this quantity is a time-reversal-even pseudoscalar, which in the present case measures the modulus and sign of the structural chirality (or helicity). Once again, the parallel with the magnetic counterparts is particularly apparent in the sequence of phase transitions we have observed in $BiCu_{0.1}Mn_{6.9}O_{12}$ (paraelectric–DDW–helical), which is completely analogous to that of frustrated magnets such as the prototypical type-II multiferroic $TbMnO_3$ (paramagnetic–SDW–cycloidal) (*26*, *27*).

One notable implication is that the $BiCu_xMn_{7-x}O_{12}$ series provides a distinctive example of emergent structural chirality acting as a macroscopic order parameter (ferrochirality). In most type-II multiferroics, including the prototypes $TbMnO_3$ (*26*–*28*) and $CaMn_7O_{12}$ (*29*, *30*), spin (vector) chirality appears below a magnetic phase transition and is coupled to improper ferroelectricity through a suitable free-energy invariant. In $TbMnO_3$, this invariant describes a direct coupling between vector spin chirality and the electric polarization and is allowed only in the weakly ferroelectric cycloidal phase, not in the high-temperature, nonpolar SDW phase (*27*, *28*). Unlike the case of $TbMnO_3$, where the magnetic chirality and electric polarization are directly coupled, multiferroicity in $CaMn_7O_{12}$ requires the presence of an additional axial structural distortion $\boldsymbol{A}$ (known as ferro-axiality) (*29*–*31*) to form the free-energy invariant $\sigma_m\boldsymbol{AP}$ (where $\boldsymbol{P}$ is the electric polarization). The above analysis leads us to the prediction that improper (weak) ferroelectricity should also be induced in $BiCu_{0.1}Mn_{6.9}O_{12}$ by precisely the same mechanism, as the free-energy invariant $\sigma_s\boldsymbol{AP}$ (with the spin chirality σ_m being replaced by the structural chirality σ_s) is allowed in the low-temperature $R3(00\gamma)t$ phase of $BiCu_{0.1}Mn_{6.9}O_{12}$.

We tested this prediction by performing ferroelectric polarization–electric field (*P*-*E*) hysteresis loop measurements (fig. S10) at the temperature of liquid nitrogen (77 K). It is

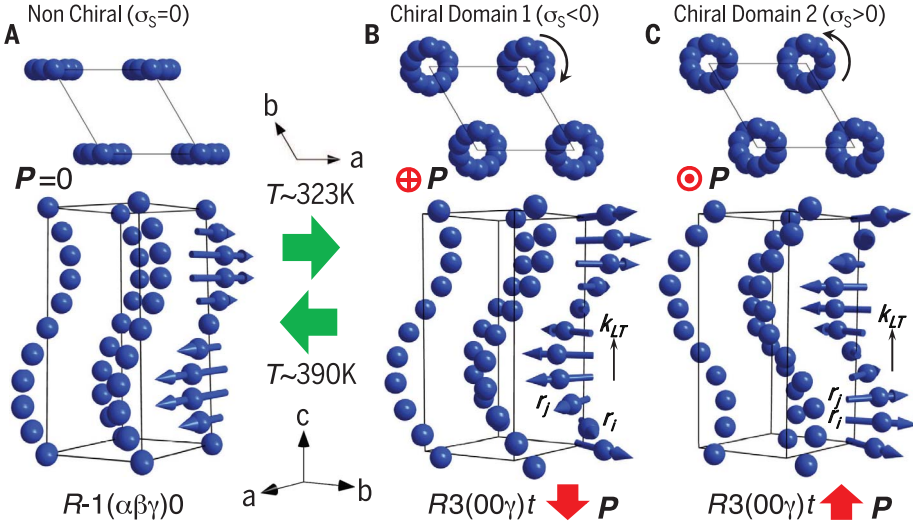

Fig. 2. Modulated atomic displacements. Schematic representation of the displacements of Bi in the (**A**) high-temperature nonchiral and (**B** and **C**) low-temperature chiral modulated phases of $BiCu_{0.1}Mn_{6.9}O_{12}$. Atoms related by *R*-centering are omitted for clarity. The black lines indicate an approximately commensurate supercell. The displacement directions are shown by arrows whose length is proportional to the magnitude of the displacement. In the chiral phase, two domains with opposite chirality, and hence opposite direction of the weak macroscopic polarization ***P***, are shown.

well known that standard *P-E* measurements can be compromised by factors unrelated to the intrinsic polarization switching, such as leakage currents (*32*). We therefore used the so-called positive-up-negative-down (PUND) method, which has been developed to distinguish true, intrinsic ferroelectric switching from artificial responses due to current leakage (*33*). The resultant *P-E* loop is consistent with the phenomenological prediction of weak improper ferroelectric polarization in the helical phase, with $|\boldsymbol{P}|$ being 4000 times smaller than the value of polarization estimated for the parent compound $BiMn_7O_{12}$ (*24*). ***P*** should, by symmetry, be directed along the *c* axis, although this could not be established for our polycrystalline samples. We note that the coexistence of ferroelectric and chiral orders is also known in smectic phases of liquid crystals with chiral molecules (*34*). These substances, however, are noncrystalline, with only directional order of anisotropically shaped molecules, giving substantially different underlying physics and materials properties.

In multiferroics, it has been shown that magnetic domains with different spin chirality can be controlled by external electric fields (*35*). By analogy, we predict that the structural chirality domains in $BiCu_{0.1}Mn_{6.9}O_{12}$ should also be controllable by an electric field, given that the polarization takes opposite directions in these domains (Fig. 2, B and C). If this controllability were to be confirmed by single-crystal or epitaxial thin films measurements, $BiCu_{0.1}Mn_{6.9}O_{12}$ would prove an unusual system in which structural chirality could be permanently switched by a static electric field. This effect would be essentially different from the electrogyration effect, in which the induced chirality has no associated hysteresis. Importantly, this functionality could be amenable to a variety of perspective applications based on materials properties associated with structural chirality (*36*, *37*), such as optical activity (a rotation of the polarization of linearly polarized light) and circular dichroism (differential absorption of left- and right-handed polarized light), particularly because the chiral phase in $BiCu_xMn_{7-x}O_{12}$ is stable up to temperatures well above room temperature.

One final question concerns the nature of orbital ordering in $BiCu_{0.1}Mn_{6.9}O_{12}$ and its relation to structural chirality. This can be established by inspecting the oxygen octahedra coordinating the B-site Mn ions in the different phases, given that differential occupancy of the e_g electronic orbitals produces unequal B-O distances within the BO_6 octahedra. The orbital state of Mn can be quantified using the mixing angle formalism proposed by Goodenough (*38*). The mixing angle θ defines an admixture between $3z^2$-r^2 and x^2-y^2 orbital states within an orbital plane, through the relation $\tan\theta = \sqrt{3}(d_{B\text{-}Oy} - d_{B\text{-}Oz})/(2d_{B\text{-}Ox} - d_{B\text{-}Oy} - d_{B\text{-}Oz})$, where $d_{B\text{-}O}$ are B-O bond lengths along *x*, *y*, or *z* direction of the local Cartesian coordinate system, as shown in Fig. 3, A to C, and E (in our analysis, we use oxygen-oxygen distances, $d_{O\text{-}O} = 2\langle d_{B\text{-}O}\rangle$, to reduce the experimental uncertainty).

As previously stated, the monoclinic phase just below T_{JT} adopts the $LaMnO_3$-type planar orbital ordering characterized by a commensurate pattern of BO_6 octahedral distortions, which gives close to fully polarized orbital states for all manganese ions (Fig. 3A). By comparison, in the triclinic DDW and the trigonal helical phases, the incommensurate atomic displacements modulate the BO_6 octahedral distortions giving rise to an incommensurate modulation of the orbital occupancy [i.e., an orbital density wave (ODW)]. The closely related quadruple perovskite $CaMn_7O_{12}$ also displays an ODW, with the orbital occupancy gradually changing between $3x^2$-r^2 and $3y^2$-r^2 along the modulation direction (*30*). In the triclinic modulated structure of $BiCu_{0.1}Mn_{6.9}O_{12}$, three out of the four symmetry-distinct Mn B-sites (Mn4, Mn5, and Mn6) display a $CaMn_7O_{12}$-type ODW (albeit in different directions) (Fig. 3B and fig. S4), whereas the Mn7 site maintains the fully polarized, unmodulated orbital state inherited from the higher-temperature monoclinic phase.

The ODW in the trigonal helical phase involves two symmetry-independent Mn B-sites, Mn2 and Mn3 (Fig. 3C and fig. S6). The latter is located on a threefold axis of symmetry, and the mixing angle θ for this site takes all values between 0° and 360° through the period of the modulation (Fig. 3, D and E). Therefore, the orbital state of the Mn3 continuously rotates in the orbital plane either clockwise or counterclockwise, following the rotation of the Bi displacements and giving rise to a chiral ODW (Fig. 3, E and F). The orbital occupancies on the Mn2 sites, which can be considered as triangular motifs interrelated by threefold symmetry, are also modulated and alternate between $3z^2$-r^2 and z^2-x^2 states (and the equivalent states obtained by threefold rotation). The phase of the modulation is not uniform on the triangle of sites, as it is in $CaMn_7O_{12}$, but instead differs by $\pm 2\pi/3$, also making the global Mn2 ODW chiral.

Thus, the orbital ordering in the hole-doped manganite $BiCu_{0.1}Mn_{6.9}O_{12}$ gradually evolves from the monoclinic $LaMnO_3$-type, commensurate phase with nearly fully polarized orbital states but disordered Bi displacements, to the incommensurate trigonal phase with chiral ODW and helical (chiral) Bi dipole displacements. The evolution takes place via an intermediate incommensurate triclinic phase combining the nonchiral Bi DDW and the nonchiral Mn ODW. This remarkable structural behavior can be interpreted as a competition between the two primary electronic instabilities, one related to the lone electron pair of Bi^{3+} and the other to the degeneracy of e_g electronic states of the octahedrally coordinated B-site Mn^{3+}—both requiring different types of structural distortions. The role of competition again underscores the analogy with magnetism, where the noncollinear spin textures appear as a result of competing exchange interactions. The apparent

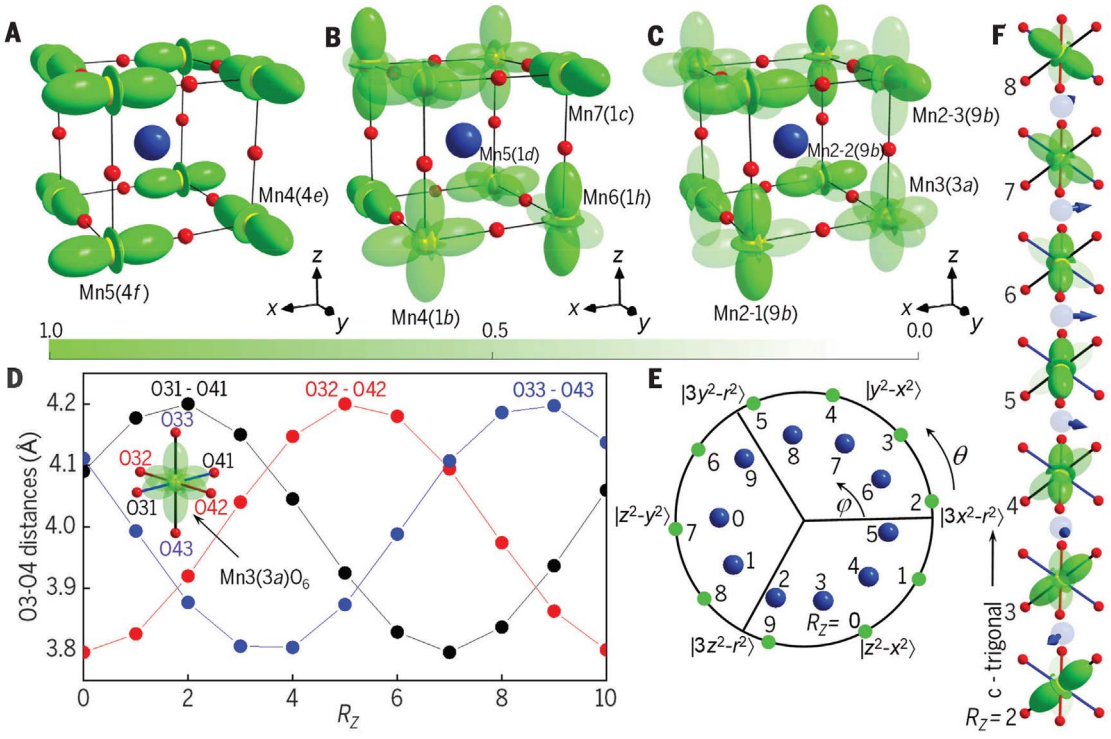

Fig. 3. Orbital ordering. Schematic representation of the B-site orbital patterns in the (**A**) monoclinic, (**B**) triclinic, and (**C**) trigonal phases of $BiCu_{0.1}Mn_{6.9}O_{12}$. For clarity, the patterns are shown relative to the familiar pseudocubic perovskite unit cell, whose edges are co-aligned with the Cartesian coordinate system (*x*, *y*, *z*) used to define the orbital states. In the triclinic (B) and trigonal (C) phases, the orbital ordering is incommensurate, and the orbital state of B-site Mn gradually changes upon propagation through the crystal. The probability of electronic occupancy for different orbitals, averaged over the modulation period, is represented by an "orbital density" (degree of transparency). In the triclinic structure, the orbital polarization changes between $|3x^2\text{-}r^2\rangle$ and $|3z^2\text{-}r^2\rangle$ for Mn4, $|3x^2\text{-}r^2\rangle$ and $|3y^2\text{-}r^2\rangle$ for Mn5, and $|3z^2\text{-}r^2\rangle$ and $|z^2\text{-}y^2\rangle$ for Mn6—a pattern that, on each site, is strongly reminiscent of $CaMn_7O_{12}$ (*30*). The Mn7 site adopts an unmodulated fully polarized $|3y^2\text{-}r^2\rangle$ state (see fig. S4 for more details). In the trigonal structure, the orbital occupancy of the Mn3 site changes between all three polarized states $|3x^2\text{-}r^2\rangle$, $|3y^2\text{-}r^2\rangle$, and $|3z^2\text{-}r^2\rangle$, making the orbital density wave chiral. The orbital polarization of the Mn2 sites in this structure changes between $|3z^2\text{-}r^2\rangle$ and $|z^2\text{-}x^2\rangle$ for Mn2-1, $|3x^2\text{-}r^2\rangle$ and $|y^2\text{-}x^2\rangle$ for Mn2-2, and $|3y^2\text{-}r^2\rangle$ and $|z^2\text{-}y^2\rangle$ for Mn2-3. In addition, the phase of the orbital modulation differs by $\pm 2/3\pi$ on these three symmetry-related sites (see fig. S5 for more details). (**D**) Oxygen-oxygen bond distances, used to characterize the anisotropy of the $Mn3O_6$ octahedra, as a function of the lattice translation $\boldsymbol{R}_Z$ along *c* axis in the trigonal phase. (**E**) Orbital states of the Mn3 site, defined by the mixing angle θ ($\tan\theta = \sqrt{3}[d_{032\text{-}042} - d_{033\text{-}043}]/[2d_{031\text{-}041} - d_{032\text{-}042} - d_{033\text{-}043}]$) (green circles), and the displacement of Bi in the *ab* plane, defined by angle φ (angle between the Bi displacement and projection of the *x* axis on the *ab* plane) (blue circles) for different values of the lattice translation $\boldsymbol{R}_Z$. To reduce the experimental uncertainty, we exploit the relation $d_{O\text{-}O} = 2\langle d_{B\text{-}O}\rangle$ for B-O bonds on either side of a given B site. (**F**) Chiral orbital density wave localized on the Mn3 site (transparency represents the probability of electronic occupation, with lower transparency corresponding to higher probability), and modulated displacements of Bi in the trigonal phase.

similarity between noncollinear electric and magnetic dipole orderings demonstrates that the formation of chiral incommensurate structures is a universal mechanism that allows a coexistence of competing degrees of freedom.

An immediate implication of the presently observed chiral electric dipole and orbital textures lies in our understanding of ferroelectric domain walls, whereby a growing number of experiments have shown that the ordering phenomenon in ferroelectric domain walls is far more complicated than previously believed (*39*–*42*). In this sense, the $BiCu_xMn_{7-x}O_{12}$ helical dipole phase can be thought of as the extended version of a ferroelectric Bloch domain boundary. In addition, by analogy with magnetism, more complex but closely related chiral objects such as electric skyrmions are likely to be feasible as well. The magnetic skyrmion lattice is often described as a multi-*k* phase represented by the superposition of three helical spin textures and induced from a single-*k* state by an external magnetic field (*43*). Electric skyrmions can be expected to also be stabilized by external stimuli or found in the domain boundaries of the $BiCu_xMn_{7-x}O_{12}$ helical phase where three single-*k* states merge together. Crucially, the formation of chiral electric dipole textures has previously been discussed only in the context of complex artificial nanostructures (*44*–*46*) or domain walls (*39*–*42*), with specific electrostatic boundary conditions or a delicate balance between electrostatic, elastic, and lattice-mismatch strain energies. Our work demonstrates a distinct approach to stabilizing these textures via competing electronic instabilities that is equally efficient for both bulk and low-dimensional structures. This perspective opens an additional dimensionality in the design of materials and suggests architectures for heterostructures, photonic crystals, and superlattices that combine traditional ingredients with components that comprise layers of chiral electric and orbital textures.

REFERENCES AND NOTES

1. J. Valasek, *Phys. Rev.* **19**, 478–491 (1922).
2. L. Néel, *Ann. Phys. (Paris)* **12**, 137–198 (1948).
3. C. G. Shull, J. S. Smart, *Phys. Rev.* **76**, 1256–1257 (1949).
4. C. Kittel, *Phys. Rev.* **82**, 729–732 (1951).
5. E. Sawaguchi, H. Maniwa, S. Hoshino, *Phys. Rev.* **83**, 1078 (1951).
6. W. C. Koehler, *J. Appl. Phys.* **32**, S20–S21 (1961).
7. W. C. Koehler, J. W. Cable, M. K. Wilkinson, E. O. Wollan, *Phys. Rev.* **151**, 414–424 (1966).
8. A. Yoshimori, *J. Phys. Soc. Jpn.* **14**, 807–821 (1959).
9. A. A. Belik *et al.*, *Inorg. Chem.* **56**, 12272–12281 (2017).
10. R. Seshadri, N. A. Hill, *Chem. Mater.* **13**, 2892–2899 (2001).
11. J. B. Neaton, C. Ederer, U. V. Waghmare, N. A. Spaldin, K. M. Rabe, *Phys. Rev. B* **71**, 014113 (2005).
12. A. A. Belik *et al.*, *Chem. Mater.* **18**, 798–803 (2006).
13. M. R. Suchomel *et al.*, *Chem. Mater.* **18**, 4987–4989 (2006).
14. J. Rodríguez-Carvajal *et al.*, *Phys. Rev. B* **57**, R3189–R3192 (1998).
15. W. A. Sławiński, H. Okamoto, H. Fjellvåg, *Acta Crystallogr. B* **73**, 313–320 (2017).
16. M. B. Salamon, M. Jaime, *Rev. Mod. Phys.* **73**, 583–628 (2001).
17. Y. Tokura, *Rep. Prog. Phys.* **69**, 797–851 (2006).

18. R. D. Johnson *et al*., *Phys. Rev. Lett.* **120**, 257202 (2018).
19. A. A. Belik, Y. Matsushita, D. D. Khalyavin, *Angew. Chem. Int. Ed.* **56**, 10423–10427 (2017).
20. See supplementary materials.
21. H. T. Stokes, D. M. Hatch, B. J. Campbell, ISOTROPY Software Suite; https://iso.byu.edu.
22. B. J. Campbell, H. T. Stokes, D. E. Tanner, D. M. Hatch, *J. Appl. Crystallogr.* **39**, 607–614 (2006).
23. V. Petricek, M. Dusek, L. Palatinus, *Z. Kristallogr. Cryst. Mater.* **229**, 345–352 (2014).
24. F. Mezzadri *et al*., *Phys. Rev. B* **79**, 100106 (2009).
25. A. Palewicz, I. Sosnowska, R. Przeniosło, A. W. Hewat, *Acta Phys. Pol. A* **117**, 296–301 (2010).
26. T. Kimura *et al*., *Nature* **426**, 55–58 (2003).
27. M. Kenzelmann *et al*., *Phys. Rev. Lett.* **95**, 087206 (2005).
28. M. Mostovoy, *Phys. Rev. Lett.* **96**, 067601 (2006).
29. R. D. Johnson *et al*., *Phys. Rev. Lett.* **108**, 067201 (2012).
30. N. J. Perks, R. D. Johnson, C. Martin, L. C. Chapon, P. G. Radaelli, *Nat. Commun.* **3**, 1277 (2012).
31. R. D. Johnson *et al*., *Phys. Rev. Lett.* **107**, 137205 (2011).
32. J. F. Scott, *J. Phys. Condens. Matter* **20**, 021001 (2008).
33. K. M. Rabe, M. Dawber, C. Lichtensteiger, C. H. Ahn, J.-M. Triscone, in *Physics of Ferroelectrics: A Modern Perspective*, K. M. Rabe, C. H. Ahn, J.-M. Triscone, Eds., vol. 105 of *Topics in Applied Physics* (Springer, 2007), pp. 1–30.
34. R. B. Meyer, L. Liebert, L. Strzelecki, P. Keller, *J. Physique Lett.* **36**, 69–71 (1975).
35. A. J. Hearmon *et al*., *Phys. Rev. Lett.* **108**, 237201 (2012).
36. P. Lodahl *et al*., *Nature* **541**, 473–480 (2017).
37. J. B. Pendry, *Science* **306**, 1353–1355 (2004).
38. J. B. Goodenough, *Magnetism and the Chemical Bond* (Interscience Publishers, John Wiley and Sons, 1963).
39. G. Catalan, J. Seidel, R. Ramesh, J. F. Scott, *Rev. Mod. Phys.* **84**, 119–156 (2012).
40. C. L. Jia, K. W. Urban, M. Alexe, D. Hesse, I. Vrejoiu, *Science* **331**, 1420–1423 (2011).
41. S. Cherifi-Hertel *et al*., *Nat. Commun.* **8**, 15768 (2017).
42. J.-Y. Chauleau *et al*., *Nat. Mater.* **19**, 386–390 (2020).
43. R. Takagi *et al*., *Sci. Adv.* **4**, eaau3402 (2018).
44. I. I. Naumov, L. Bellaiche, H. Fu, *Nature* **432**, 737–740 (2004).
45. A. K. Yadav *et al*., *Nature* **530**, 198–201 (2016).
46. S. Das *et al*., *Nature* **568**, 368–372 (2019).
47. D. D. Khalyavin *et al*., Experimental data for emergent helical texture of electric dipoles, Version 1, Zenodo (2020); https://doi.org/10.5281/zenodo.3749292.

ACKNOWLEDGMENTS

We thank Y. Katsuya, M. Tanaka, and Y. Matsushita of NIMS for their help with synchrotron x-ray and SEM data collections. The synchrotron radiation experiments were performed at SPring-8 with the approval of the NIMS Synchrotron X-ray Station (proposal numbers: 2016B4504 and 2017A4503). The authors also acknowledge the Science and Technology Facility Council for the provision of neutron beam time on the WISH instrument (RB1810030). **Funding:** R.D.J. acknowledges support from a Royal Society University Research Fellowship. A.A.B. acknowledges partial support from grant JPJ004596 (ATLA, Japan). **Author contributions:** D.D.K. and F.O. performed interpretation and refinement of the neutron and x-ray diffraction data collected by P.M. and A.A.B. at different facilities. R.D.J. and P.G.R. suggested the symmetry principles of coupling between structural chirality and macroscopic polarization and performed (*P-E*) measurements. A.A.B. developed the concept, carried out the materials synthesis, characterization, and physical property measurements. All authors contributed to the preparation of the manuscript and to discussion of the results. **Competing interests:** The authors declare no competing interests. **Data and materials availability:** The experimental data used in this study are available at Zenodo (*47*).

SUPPLEMENTARY MATERIALS

science.sciencemag.org/content/369/6504/680/suppl/DC1
Materials and Methods
Figs. S1 to S10
Tables S1 to S5
References (*48*–*50*)

17 July 2019; accepted 12 June 2020
10.1126/science.aay7356

Science

Emergent helical texture of electric dipoles

Dmitry D. Khalyavin, Roger D. Johnson, Fabio Orlandi, Paolo G. Radaelli, Pascal Manuel and Alexei A. Belik

Science **369** (6504), 680-684.
DOI: 10.1126/science.aay7356

A helix of dipoles

In magnetic materials, magnetic dipoles typically line up parallel or antiparallel to each other. However, more complex orderings, such as helical, can also occur. Khalyavin *et al.* found that in the material $BiCu_{0.1}Mn_{6.9}O_{12}$, a helical order can be formed out of electric rather than magnetic dipoles. The material also harbors an associated structural helical order, which symmetry analysis suggests might be switchable with an applied electric field.

Science, this issue p. 680

Science (print ISSN 0036-8075; online ISSN 1095-9203) is published by the American Association for the Advancement of Science, 1200 New York Avenue NW, Washington, DC 20005. The title *Science* is a registered trademark of AAAS.